

# Scalable High-Performance Algorithm for the Simulation of Exciton Dynamics. Application to the Light-Harvesting Complex II in the Presence of Resonant Vibrational Modes

Christoph Kreisbeck,<sup>\*,†</sup> Tobias Kramer,<sup>\*,‡</sup> and Alán Aspuru-Guzik<sup>\*,¶</sup>

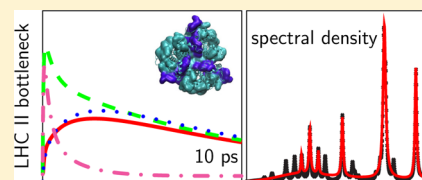
<sup>†</sup>Institut für Physik, Humboldt-Universität zu Berlin, Newtonstr. 15, 12489 Berlin, Germany

<sup>‡</sup>Mads Clausen Institute, University of Southern Denmark, Alsion 2, 6400 Sønderborg, Denmark

<sup>¶</sup>Department of Chemistry and Chemical Biology, Harvard University, 12 Oxford Street, Cambridge, Massachusetts 02138, United States

## S Supporting Information

**ABSTRACT:** The accurate simulation of excitonic energy transfer in molecular complexes with coupled electronic and vibrational degrees of freedom is essential for comparing excitonic system parameters obtained from ab initio methods with measured time-resolved spectra. Several exact methods for computing the exciton dynamics within a density-matrix formalism are known but are restricted to small systems with less than 10 sites due to their computational complexity. To study the excitonic energy transfer in larger systems, we adapt and extend the exact hierarchical equation of motion (HEOM) method to various high-performance many-core platforms using the Open Compute Language (OpenCL). For the light-harvesting complex II (LHC II) found in spinach, the HEOM results deviate from predictions of approximate theories and clarify the time scale of the transfer process. We investigate the impact of resonantly coupled vibrations on the relaxation and show that the transfer does not rely on a fine-tuning of specific modes.



## 1. INTRODUCTION

The excitonic energy transfer in light-harvesting complexes starts with the excitation of an electronic state. The excited system is out of thermal equilibrium with the molecular environment, which couples the electronic degrees of freedom to the vibrational modes. The excitons transverse the molecular network consisting of pigments such as (bacterio)chlorophylls toward the thermal equilibrium populations at the network sites. Understanding these processes requires the development of a coupled system-bath model, referred to as *open quantum system*. For light-harvesting complexes, usually these models are based on the Frenkel-exciton description.<sup>1–3</sup>

With the availability of femtosecond laser sources for triggering the excitation, a detailed, quantitative experimental study of the transport sequence has been achieved with time-resolved two-dimensional (2D) echo spectra and transient absorption spectra. The recorded 2D echo spectra of the Fenna–Matthews–Olson (FMO) complex<sup>4–6</sup> and the light-harvesting complex II (LHC II)<sup>7</sup> contain a wealth of information and show the dissipative nature of the excitonic transport in form of the movement of peak intensity from the initially excited states along the diagonal of the 2D spectra toward lower-energy, off-diagonal locations.<sup>4</sup> On top of the relaxation process, oscillatory components prevail in 2D spectra, which contain signatures of electronic coherences and specific vibrational modes.<sup>6,8–10</sup>

The coupling to the environment determines the transfer efficiency in LHCs<sup>11,12</sup> through the bath-correlation time of the phonon bath,<sup>13–15</sup> the shape of the continuum part of the spectral density,<sup>9,16</sup> and specific structures within the spectral

density.<sup>9,17</sup> For the FMO complex, the superohmic character of the spectral density results in long-lasting electronic coherences despite a strong coupling to the environment.<sup>9</sup> To investigate to what extent specific modes in the spectral density affect transfer time scales in larger light-harvesting networks calls for efficient methods to calculate the exciton dynamics for realistic spectral densities. Several accurate computational methods for obtaining the transfer dynamics have been developed, but their application to larger systems is either hindered by their long run-times, often exceeding days for a dimer system, or limited to structureless spectral densities.<sup>18,19</sup>

Here, we introduce the *QMaster*-tool for high-performance computations of open-system dynamics across a wide range of parallel accelerators, including large-memory devices. As shown previously, the hierarchical equation of motion (HEOM) method shows excellent scalability on graphics processing units (GPU) processors<sup>15,20</sup> and has been the only tool employed to date to compute 2D spectra of the FMO complex for structured spectral densities.<sup>9</sup> The GPU-HEOM tool is publicly available as a ready-to-run cloud computing tool hosted on the nanohub platform.<sup>21</sup> For studying systems larger than the FMO complex, the GPU approach is limited by the available memory on the GPU device. The advantage of the *QMaster*-tool lies in the flexibility to run HEOM on different hardware architectures comprising multicore CPUs, GPUs, and the Intel XeonPhi accelerator. This flexibility allows one to choose the compute

Received: July 17, 2014

Published: August 18, 2014

hardware according to the needs for the investigated system and to benefit from the high-compute throughput provided by GPUs as well as from the large memory found in multicore CPU workstations.

We deploy the *QMaster*-tool to accurately model the time scale of excitonic energy transfer in LHC II found in spinach,<sup>22</sup> which is part of the photo- and antenna-system of higher plants.<sup>23–25</sup> LHC II consists of three monomeric units with 14 chlorophylls (Chl), further divided into two types Chla/Chlb. Energy transfer in LHC II works by a transfer and relaxation process between both chlorophyll types. Besides the larger number of chlorophylls (14 Chl per monomeric unit in LHC II, compared to 7 bacteriochlorophylls in FMO), also the spectral density of LHC II is highly structured with more than 48 vibrational peaks revealed by fluorescence line narrowing spectroscopy.<sup>26,27</sup> To investigate the impact of peaks in the spectral density on the transfer dynamics, we include several underdamped vibrational modes in the calculations. There is an ongoing debate if underdamped modes in LHCs are tuned to resonance to enhance the transfer efficiency.<sup>28,29</sup> It has been suggested that nonclassical phenomena and vibration-assisted transfer through resonantly coupled underdamped modes enhances Chlb/Chla interband relaxation in LHC II.<sup>29</sup> For the Fenna–Matthews–Olson (FMO) complex and dimer models computations with HEOM and the quasi-adiabatic path integral (QUAPI) show that added underdamped modes act as additional dissipative channels, which do not alter the transfer efficiency appreciably.<sup>16,30,31</sup> However, 2D echo spectra are more susceptible to vibrational modes and reflect both electronic and vibrational effects.<sup>10</sup>

Due to the lack of computational capabilities, energy transfer in LHC II had been previously calculated only with approximate methods<sup>32–34</sup> with nonconclusive results for the transfer time scales. The predictions for the relaxation time differ by more than 1 order of magnitude<sup>27,32,35–37</sup> from the results of Renger et al.<sup>34</sup> The site energies have been previously derived by modeling experimental data with different approximate theories and result in different sets of parameters for the LHC II system,<sup>35,38</sup> see the Supporting Information (SI). The increased accuracy of the dynamical model with *QMaster* motivates future refinements of parameter sets to obtain a consistent model encompassing the various experimental data, including time-resolved, 2D echo spectra, and hole-burning data.<sup>39</sup>

Approximate methods work best in specific limits of delocalized (Redfield type) or incoherent dynamics (Förster transfer), or alternatively try to interpolate between the two cases. Any interpolation and combination of Förster/Redfield methods requires the introduction of an empirical cutoff parameter, which depends on the precise system parameters (excitonic energies) as well as on the environment (temperature). The optimal value for the cutoff parameter is *a priori* unknown. In contrast to the approximate methods, HEOM does work across the full range of coupling strengths<sup>40</sup> and includes the effects of dynamic localization due to the reorganization process.<sup>36</sup>

In section 2, we discuss the underlying design of the software stack for separating the performance-critical accelerated routines (*kernels*) from the high-level object-oriented framework, supporting sustainable software development<sup>41</sup> and paving the way for accurate simulations of larger light-harvesting systems. We demonstrate that with small modifications the same algorithm runs efficiently across different many-core devices and at the same time takes advantage of the specific device features.

The Frenkel exciton model is setup in section 3 to investigate the effects of structures in the spectral density on energy transfer times in LHC II (section 4). In section 5, we calculate the relaxation time scale in LHC II and discuss short-comings of previous approximative results. Finally, we outline future developments and give additional details of the algorithm and the implementation in the appendix.

## 2. ALGORITHM DESIGN FOR HIGH-PERFORMANCE ACCELERATORS

A significant component of the supercomputing infrastructure is currently transitioning to massively parallel many-core accelerators already built into single servers, rather than solely relying on network-linked CPU cores. Besides GPU accelerators, Intel released 2013 the first Many Integrated Core (Intel-MIC) device, the Xeon Phi. Existing programs and standard algorithms have been optimized over decades for conventional CPU systems and are not directly able to take advantage of new accelerator architectures.<sup>42</sup>

For studying the dynamics in open quantum systems, two many-core enabled tools have been implemented and are publicly available for users: (i) GPU-HEOM for solving the hierarchical equations of motions on graphics processing units (GPU)<sup>15,21</sup> and (ii) the parallel hierarchy integrator (*phi-tool*) for multicore CPU systems.<sup>19</sup> The *phi-tool* and GPU-HEOM follow different performance strategies and target different applications. The *phi-tool* makes use of the large system memory available in workstations to compute the exciton dynamics for instance in the light-harvesting complexes LH 2 (B850 ring) and LH 1 (B875 ring), a combined 50-sites system, which requires up to 108 GB of memory.<sup>19</sup> The *phi-tool* is tied to a structureless Drude-Lorentz shape of the spectral density and to the propagation of a density-matrix specified at the initial time. GPU-HEOM is more flexible in the calculation modes<sup>21</sup> and utilizes the high compute-throughput of modern GPUs for the efficient computation of numerically intense 2D echo spectra of the FMO complex.<sup>9,10</sup> The application of GPU-HEOM is restricted by the amount of GPU device memory (6 GB or 12 GB on the current Nvidia K20/K40 GPU). Although the GPU memory steadily increases, Figure 1 shows that extending the

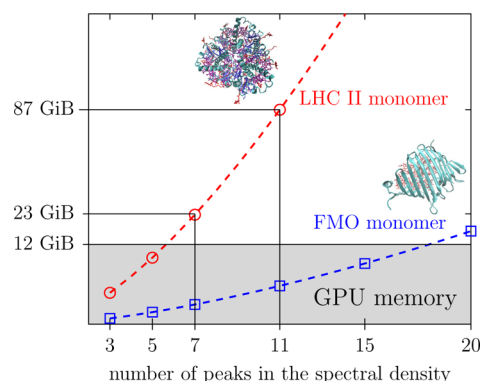


**Figure 1.** Scaling of the required device memory of GPU-HEOM/*QMaster* simulations with increasing number of peaks in the spectral density for a 14-site LHC II-monomer and a 7-site FMO monomer. The hierarchy truncation level is set to  $N_{\max} = 3$ , a typical value required for treating structured spectral densities<sup>9</sup> at physiological temperatures. Increasing the truncation depth increases the memory consumption further. The gray area represents the device memory of the Nvidia K40 GPU platform.

complexity of the spectral density (indicated by the number of peaks in the spectral density) quickly exhausts the available memory. Two strategies are available to overcome the memory bottleneck: (i) a multidevice method, which distributes memory across different devices, or (ii) a move to non-GPU accelerators with larger memory. The first approach introduces a considerable overhead to manage the distributed memory and the program flow. In addition one needs to reduce the time-consuming memory transfers across the connected computers by partly duplicating the memory contents (“halo technique”<sup>43</sup>). The *QMaster*-tool follows the second strategy by using the Open Compute Language (OpenCL) to maintain a common-code basis over all supported accelerator devices, while still taking advantage of device specific features. The cross-platform performance of *QMaster* is shown in Figure 2a, which charts the compute time

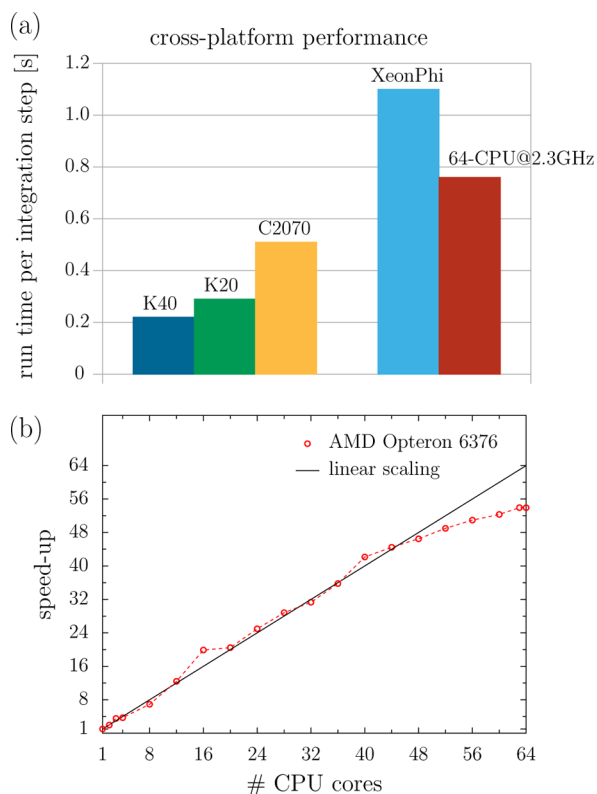


**Figure 2.** Average computation time of *QMaster* for one Runge–Kutta fourth-order integration step. Parameters used: spectral density  $J_{3\text{peaks}}$ , hierarchy truncation at  $N_{\text{max}} = 3$ , resulting in 105 995 auxiliary matrices and 1.9 GB memory consumption. (a) *QMaster* performance across different OpenCL platforms. The K40, K20, C2070 GPU devices show the best performance, followed by the AMD Opteron 64 CPU-cores setup. The Xeon Phi system does not reach its theoretically possible peak performance. (b) Speedup of HEOM on the AMD Opteron 64-core CPU system as a function of active cores, controlled by the OpenCL device-fission extension.

for one propagation step of the density matrix representing the monomeric unit of LHC II consisting of 14 chlorophylls (hierarchy truncation at  $N_{\text{max}} = 3$ , spectral density  $J_{3\text{peaks}}$ ). In this case, the HEOM approach utilizes 105 995 auxiliary matrices which consume 1.9 GB of memory. The same code is run across different devices, including the Nvidia C2070, K20 and K40 GPUs, the Intel Xeon-Phi, and an AMD Opteron 6376 64-core CPU system. The best absolute performance is measured on the GPU systems. The advances in GPU technology are manifest in

the steady performance gains seen by using newer GPU devices. From the release of the C2070 GPU at the end of 2010 to the K40 Kepler generation, one finds a 2.3-fold reduction in computation time per propagation step from 0.51 s (C2070) to 0.22 s (K40). Although the XeonPhi has a similar theoretical peak performance for double-precision floating point operations as the K40, the XeonPhi runs about 5 times slower. We attribute this to missing vectorization and optimization paths of the OpenCL compiler and note that similar effects are also seen in other benchmark calculations.<sup>42</sup> One important finding is the excellent performance of the OpenCL HEOM-kernels on the 64-core AMD Opteron 6376 processor. The AMD processor resides in a workstation with 252 GB main memory and is therefore suitable for computations with large memory requirements. To analyze the scaling of *QMaster* with the number of active CPU cores, we employ the device-fission extension of OpenCL and increase successively the number of active cores. Figure 2b shows the speedup of multicore runs compared to a single-core run. *QMaster* scales linearly up to 48 cores before the curve starts to saturate. By utilizing all 64 available cores, we obtain a 54-fold speedup. OpenCL reserves one core for instructions of the operating system, and there is no difference between using 63 and 64 cores.

The modular *QMaster*-tool has been developed around the design principle of a single propagation thread executing on the host system, which delegates the execution to the attached many-core device. The propagation thread follows the time evolution of the quantum-mechanical systems interacting with the vibrational environment. Depending on the calculation mode, the user schedules different events on the propagation thread, for instance a sequence of pump–probe laser pulses. When a previously registered event is executed, the standard forward propagation on the accelerator is interrupted and for instance the dipole operator of the laser field is applied to the quantum system stored on the accelerator. After completing the event handling, the propagation thread resumes. Additional extensions of the standard Hamiltonian are optionally attached to the propagation thread, such as exciton trapping sites and general loss channels. The chosen setup ensures that the performance-critical kernels run most of the time uninterrupted and exclusively on the accelerator device.

### 3. MODELING EXCITON DYNAMICS IN LHC II

We use *QMaster* to accurately determine the time scale of energy relaxation from the high energy Chlb band to the low energy Chla band within one monomeric of LHC II. The model follows the standard Frenkel-exciton description of light-harvesting complexes within the single exciton manifold.<sup>3</sup> The Hamiltonian in the site basis denoted by  $|m\rangle$  (each Chl constitutes one site of the  $N$ -sites complex) is

$$\mathcal{H}_{\text{ex}} = \sum_{m=1}^N \epsilon_m^0 |m\rangle\langle m| + \sum_{m>n} J_{mn} (|m\rangle\langle n| + |n\rangle\langle m|) \quad (1)$$

The parameters for the  $N = 14$  LHC II site energies and the intersite couplings  $J_{mn}$  are given in the SI for two different models of the LHC II complex.<sup>35,38</sup> At each site, the electronic state is coupled to molecular vibrations, which are characterized by a set of harmonic oscillators

$$\mathcal{H}_{\text{phon}} = \sum_{m,i} \hbar \omega_{i,m} b_{i,m}^\dagger b_{i,m} \quad (2)$$



We assume a linear coupling of the exciton system to the vibrations and uncorrelated vibrations at different sites:

$$\mathcal{H}_{\text{ex-phon}} = \sum_m |m\rangle \langle m| \sum_i \hbar \omega_{i,m} d_{i,m} (b_{i,m} + b_{i,m}^\dagger) \quad (3)$$

The reorganization energy  $\mathcal{H}_{\text{reorg}} = \sum_m \lambda_m |m\rangle \langle m|$  with  $\lambda_m = \sum_i \hbar \omega_{i,m} d_{i,m}^2 / 2$  is added to the site energy  $\epsilon_m^0$ . The frequency-dependent coupling strength is given by the spectral density

$$J_m(\omega) = \pi \sum_i \hbar^2 \omega_{i,m}^2 d_{i,m}^2 \delta(\omega - \omega_{i,m}) \quad (4)$$

The form of the spectral density  $J(\omega)$  for LHC II is modeled upon data from fluorescence line narrowing spectroscopy<sup>44</sup> ( $J_{\text{LHC II}}$ , Figure 3). The measured structured peaks in the spectral density are contained in different parametrizations and added on top of the background function  $J_R$ , taken from ref 38, SI, eq S9

$$J_R(\omega) = \frac{0.5\hbar\omega^2\pi}{(s_1 + s_2)} \sum_{i=1,2} \frac{s_i \omega^3 e^{-\sqrt{\omega/\omega_i}}}{7!2\omega_i^4}, \quad s_{1,2} = \{0.8, 0.5\},$$

$$\omega_{1,2} = \{0.56, 1.94\} \text{cm}^{-1} \quad (5)$$

The background spectral density  $J_R$  contributes about 40  $\text{cm}^{-1}$  to the reorganization energy  $\hbar\lambda_m = \int_0^\infty d\omega (J_m(\omega)/(\pi\omega))$  and the 20 additional peaks located within the range of excitonic eigenenergy differences result in the combined reorganization energy of 216  $\text{cm}^{-1}$ .  $J_{\text{LHC II}} = J_R + J_{\text{BO}}$  is given as a superposition of underdamped Brownian oscillators with parameters from ref 45, SI, Table S9

$$J_{\text{BO}}(\omega) = 2\hbar \sum_j S_j \Omega_j^3 \frac{\omega \nu_{\text{vib}}}{(\Omega_j^2 - \omega^2)^2 + \omega^2 \nu_{\text{vib}}} \quad (6)$$

with  $\hbar\nu_{\text{vib}} = 10 \text{ cm}^{-1}$ . To apply HEOM computationally efficient, a decomposition of the spectral density into multiple hierarchies is required.<sup>9,46</sup> To this end, we parametrize the spectral density as a sum over  $N$  shifted Drude–Lorentz peaks

$$J_{N\text{peaks}}(\omega) = \sum_{k=1}^N \left( \frac{\nu_k \lambda_k \omega}{\nu_k^2 + (\omega + \Omega_k)^2} + \frac{\nu_k \lambda_k \omega}{\nu_k^2 + (\omega - \Omega_k)^2} \right) \quad (7)$$

Figure 3 details the spectral density of LHC II and various decompositions as sum of shifted Drude–Lorentz peaks, which reflect different levels of approximations to  $J_{\text{LHC II}}$ .

*QMaster* solves the exciton dynamics on the basis of an extension of the hierarchical coupled equations of motion approach (HEOM) to structured spectral densities.<sup>9,47</sup> The reduced density matrix is obtained by tracing out the vibrational degrees of freedom from the density matrix  $R(t)$  of the combined system and vibrational bath Hamiltonian  $\mathcal{H} = \mathcal{H}_{\text{ex}} + \mathcal{H}_{\text{phon}} + \mathcal{H}_{\text{ex-phon}}$

$$\rho(t) = \text{tr}_{\text{vibrations}} R(t) \quad (8)$$

The HEOM method for obtaining  $\rho(t)$  is described in detail elsewhere.<sup>14,47–49</sup> Here, we focus on the performance critical parts of the algorithm and discuss strategies for achieving high performance across different accelerator devices, including GPUs.<sup>15</sup> For large systems and complex spectral densities, HEOM requires the integration of a system of up to several millions of auxiliary density matrices  $\sigma^{\vec{n}}$ , where the member  $\sigma^{\vec{0}} \equiv \rho(t)$  denotes the reduced density matrix. The equation of motion for the reduced density matrix becomes

$$\begin{aligned} \frac{d}{dt} \rho(t) = & -\frac{i}{\hbar} [\mathcal{H}_{\text{ex}}, \rho(t)] \\ & - \sum_{m,k=1,s=\pm 1}^{N,M} \frac{2}{\beta \hbar^2} \frac{\lambda_k \nu_k}{(\gamma_1 + i s \Omega_k)^2 - \nu_k^2} V_m^\times V_m^\times \rho(t) \\ & - \sum_{m,k=1,s=\pm 1}^{N,M} n_{m,k,s} (\nu_k + i s \Omega_k) \rho(t) \\ & + \sum_{m,k=1,s=\pm 1}^{N,M} \frac{i}{\hbar} V_m^\times \sigma^{\vec{n}_{m,k,s}}(t), \end{aligned} \quad (9)$$

and the interlinked hierarchy is propagated by solving

$$\begin{aligned} \frac{d}{dt} \sigma^{\vec{n}}(t) = & -\frac{i}{\hbar} [\mathcal{H}_{\text{ex}}, \sigma^{\vec{n}}(t)] \\ & - \sum_{m,k=1,s=\pm 1}^{N,M} \frac{2}{\beta \hbar^2} \frac{\lambda_k \nu_k}{(\gamma_1 + i s \Omega_k)^2 - \nu_k^2} V_m^\times V_m^\times \sigma^{\vec{n}}(t) \\ & - \sum_{m,k=1,s=\pm 1}^{N,M} n_{m,k,s} (\nu_k + i s \Omega_k) \sigma^{\vec{n}}(t) \\ & + \sum_{m,k=1,s=\pm 1}^{N,M} \left( \frac{i}{\hbar} V_m^\times \sigma^{\vec{n}_{m,k,s}}(t) + \theta_{m,k,s} \sigma^{\vec{n}_{m,k,s}}(t) \right), \end{aligned} \quad (10)$$

with operators

$$\begin{aligned} \theta_{m,k,s} = & \frac{i}{2} \left( \frac{2\lambda_k}{k_B T \hbar} V_m^\times - i \lambda_k (\nu_k + i s \Omega_k) V_m^\circ \right. \\ & \left. - \frac{2\lambda_k}{\beta \hbar^2} \frac{(\nu_k + i s \Omega_k)^2}{\gamma_1^2 - (\nu_k + i s \Omega_k)^2} V_m^\times \right) \end{aligned} \quad (11)$$

and

$$V_m^\times \sigma = [ |m\rangle \langle m|, \sigma ], \quad V_m^\circ \sigma = [ |m\rangle \langle m|, \sigma ]_+ \quad (12)$$

The index  $\vec{n}$  of the auxiliary matrix  $\sigma^{\vec{n}}$  is defined as tuple

$$\vec{n} = (n_{1,1,+}, n_{1,1,-}, \dots, n_{1,M,+}, n_{1,M,-}, \dots, n_{N,M,+}, n_{N,M,-}) \quad (13)$$

where  $n_{m,k,\pm} \in \mathbb{N}$ . The first index  $m = 1, \dots, N$  runs over sites, the second one  $k = 1, \dots, M$  covers the number of shifted Drude–Lorentz peaks, and the  $s = \pm$  denotes the sign of the frequency shift  $\pm \Omega_k$ . We further define  $\vec{n}_{m,k,s}^\pm = (n_{1,k,s}^\pm, \dots, n_{m,k,s}^\pm, \dots, n_{N,M,s}^\pm)$ . For computational efficiency, we split eq 10 into three parts, according to the alignment between the hierarchy members  $\sigma^{\vec{n}}$  on the l.h.s. and the r.h.s. The evaluation of the commutator  $[\mathcal{H}_{\text{ex}}, \sigma^{\vec{n}}(t)]$  for all hierarchy members entails many matrix–matrix multiplications between a constant matrix representing  $\mathcal{H}_{\text{ex}}$  and all hierarchy matrices. For this step, the memory locations of input and output hierarchy members are aligned, which increases the data throughput. The hierarchy members coupled in the next part of eq 10 are stored at two different locations  $\sigma^{\vec{n}_\pm}$ , and this results in a partly non-contiguous memory-access pattern. To reduce the impact of unaligned operations, we store the elements of each hierarchy matrix contiguously and take advantage of data prefetching (Appendix A).

The hierarchy converges for sufficiently large values  $\sum_{m,k,s} n_{m,k,s}$  and we terminate the hierarchy if the condition  $\sum_{m,k,s} n_{m,k,s} > N_{\max}$  is fulfilled. Convergence can be either tested by comparing deviations in the dynamics for different truncation levels or tested against the analytically known absorption spectra of a single chromophore, which is given in terms of integrals involving solely the bath-correlation function  $C(t)$ .<sup>50–53</sup> The HEOM method implements for computational efficiency a high-temperature approximation (HTA) for the real part of  $C(t)$ , leading to slight deviations from the analytical results (Appendix B).

#### 4. INFLUENCE OF THE VIBRATIONAL PEAKS ON THE TRANSPORT IN LHC II

The peaks contained in the spectral density of LHC II reflect underdamped vibrational modes, which are for specific disorder realizations of the exciton Hamiltonian close to resonance with the exciton eigenenergy differences (dashes in Figure 3).

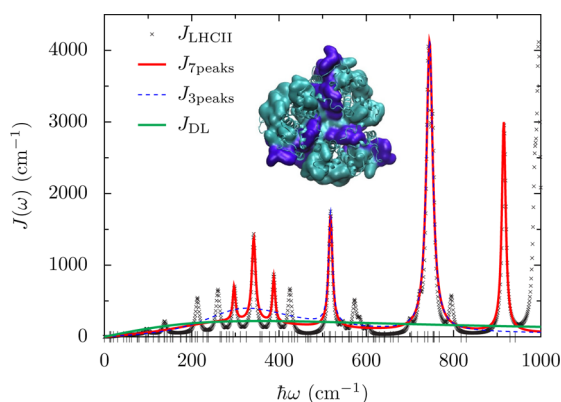


**Figure 3.** Spectral density  $J(\omega)$  for the LHC II monomer in different parametrizations. For the calculations  $J_{3\text{peaks}}$  with  $\lambda = \{161, 16, 48\} \text{ cm}^{-1}$ ,  $\nu^{-1} = \{40, 1000, 600\} \text{ fs}$ ,  $\Omega = \{300, 518, 745\} \text{ cm}^{-1}$ ,  $J_{7\text{peaks}}$  with  $\lambda = \{130, 6, 18, 6, 16, 48, 17\} \text{ cm}^{-1}$ ,  $\nu^{-1} = \{30, 1400, 1000, 1400, 1000, 600, 1000\} \text{ fs}$ ,  $\Omega = \{240, 297, 342, 388, 518, 745, 915\} \text{ cm}^{-1}$  and  $J_{\text{DL}}$  with  $\lambda = 220 \text{ cm}^{-1}$ ,  $\nu^{-1} = 15 \text{ fs}$ ,  $\Omega = 0$  are used.  $J_{\text{RG}}$ ,  $J_{\text{RR}}$  are parametrizations based on the fluorescence line-narrowing data described in the text. Dashes on the horizontal axis mark the energy difference  $\Delta E_{ij}$  of the exciton eigenstates of the LHC II monomer. The inset shows the trimeric assembly of LHC II.<sup>22</sup>

It has been suggested that the vibrations might be tuned in resonance in order to improve interband energy transfer from the energetically higher-lying Chlb sites to the Chla band.<sup>29</sup> An experimental assessment of the impact of specific vibrational modes by 2D echo spectroscopy is complicated due to superposition of ground-state vibrations and excited-state absorption signals on top of the stimulated emission pathway, which for specific systems overshadow electronic coherences.<sup>10,54</sup> For the FMO complex, added resonant modes hardly diminish or enhance transfer efficiencies.<sup>16,30</sup> Previous works focus on dimer pairs as representatives for Chlb/Chla transfer-pathways in LHC II and suggest nonclassical phenomena and vibration-assisted transfer in the model system.<sup>29</sup> A typical dimer pair is given by Chlb 601 and Chla 602 with an energy splitting chosen close to resonance with the intramolecular vibration peak at  $\Omega_{\text{vib}} = 742 \text{ cm}^{-1}$ .

With *QMaster* an accurate investigation of LHC II transfer dynamics beyond a dimer model is possible and allows to assess the relative importance of specific vibrational modes.

The simulation encompasses all 14 sites of the monomeric LHC II unit and adds up to six vibrational peaks on top of the background spectral density, including the resonant vibrational mode with frequency  $\Omega = 745 \text{ cm}^{-1}$ . To distinguish the influence of specific modes for LHC II, we consider distinct forms of the spectral density, denoted by  $J_{7\text{peaks}}$ ,  $J_{3\text{peaks}}$ , and  $J_{\text{DL}}$  parameters given in Figure 3.  $J_{7\text{peaks}}$  constitutes the most detailed spectral density model, while  $J_{3\text{peaks}}$  interpolates over fine-structure around  $350 \text{ cm}^{-1}$ . In addition, a single-peak, nonshifted Drude–Lorentz spectral density  $J_{\text{DL}}$  is included in the comparison. All spectral densities cover the energy range spanned by the exciton energy differences  $\Delta E_{ik} = |E_i - E_k|$ , where  $E_i$  denotes the exciton energies of the LHC II monomer. The values of  $\Delta E_{ik}$  are marked by the dashes on the energy axis in Figure 3. As an initial condition, we consider an excitation of the highest exciton eigenstate, which is mainly localized at the Chlb 606 site (the nomenclature follows ref 22). We first discuss the LHC II parameter set based on ref 35 (SI, Table 1) and track in Figure 4 the aggregated excitation of the Chlb sites

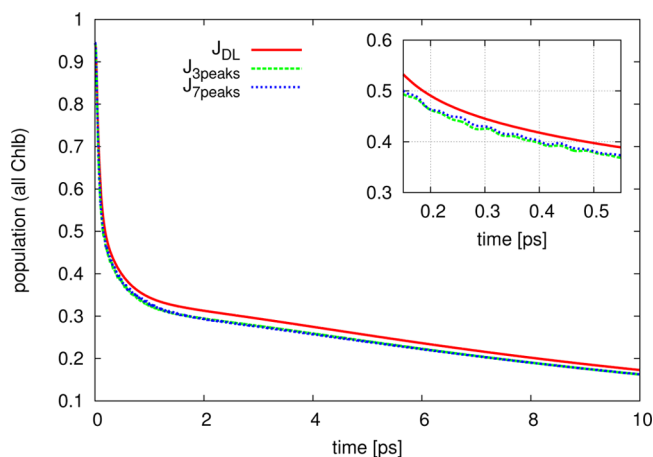


**Figure 4.** HEOM calculation of the population dynamics in LHC II with initial population of the highest eigenstate for different spectral densities in Figure 3 for  $T = 300 \text{ K}$ . Shown is the aggregated population of all Chlbs as a function of time. The inset shows the effect of underdamped modes in  $J_{\{3,7\}\text{peaks}}$  on the population dynamics.

(601, 605, 606, 607, 608, and 609). The relaxation proceeds in a very similar way for all investigated spectral densities  $J_{\{3,7\}\text{peaks}}$  and  $J_{\text{DL}}$  at  $T = 300 \text{ K}$ . Initially, there is a fast decay from the high energy Chlb's to the low energy Chla's. Around  $0.2 \text{ ps}$  the population of the Chlb's drops below  $0.5$ . Afterward, a slow decay prevails, and then a steady thermal state is reached after  $50 \text{ ps}$  for  $J_{\text{DL}}$ . The slower decay is caused by bottleneck effects discussed in sec 5. For simplicity and to demonstrate better the specific features of each spectral density, no average over static disorder is performed. The distinct peaks in the spectral densities  $J_{3\text{peaks}}$  and  $J_{7\text{peaks}}$  lead to small-amplitude oscillations in the population dynamics (Figure 4, inset). The relaxation time scale is not affected by specific peaks in the spectral density and already the featureless spectral density  $J_{\text{DL}}$  reproduces the relaxation dynamics seen with the structured models  $J_{\{3,7\}\text{peaks}}$ .

The specific form of the continuum part of the spectral density in turn has a stronger impact on the transfer pathways and on the duration of electronic coherences. A careful measurement of the overall form of the spectral density is essential for the accurate modeling of light-harvesting complexes.<sup>55,56</sup> A coarse-grained description of the transfer with a coupling to a

continuum of phonon modes provides a good description of the transport provided that three criteria are fulfilled: (i) the reorganization energy is in the same order of magnitude as the spectral density of LHC II, (ii) the spectral density covers the energy range spanned by the differences of the exciton energies to provide dissipative channels. In addition, the slope of the spectral density toward zero frequency affects the transport through the pure-dephasing rate.<sup>9,16</sup> In LHC II, the form of  $J_{DL}$  fulfills these criteria and thus provides a useful coarse-grained representation of the spectral density to assess the transport dynamics. This finding mirrors the results found in the transport analysis of the FMO complex<sup>9,16</sup> and demonstrates that no fine-tuning of specific vibrational modes is required to sustain robust and efficient environmentally assisted energy transfer.<sup>11,12,57</sup>

## 5. CHLB/CHLA TRANSFER TIME SCALE IN LHC II

Next, we compare various approximate methods to the *QMaster* results for the time scale of the exciton dynamics in LHC II. Approximate methods play an important role for deriving estimates for the transfer dynamics in photosynthetic networks comprising several hundred chlorophylls, which are out of reach for exact methods.

LHC II has been extensively studied within the Redfield, Förster, and interpolating approximations. Without an exact solution of the open system dynamics obtained with *QMaster*, the error made by the approximate methods is undefined and it is not known which approximation works best for a specific system. Test calculations using HEOM for dimers show that the HEOM dynamics approaches the Redfield theory for small couplings between the chromophores and the vibrational bath, whereas for very large couplings, HEOM yields the expected Förster rates.<sup>14</sup> The ability of HEOM to accurately handle the intermediate parameter regime encountered in light-harvesting complexes establishes HEOM as a reference standard within the field of excitonic energy transfer in photosynthesis.<sup>36</sup>

HEOM calculations show that in the photosynthetic system of purple bacteria, the intercomplex transfer between LH1 rings and the reaction center (RC) is well-described within the Förster picture.<sup>18</sup> This finding is tied to the LH1 system and does not carry over to the case of LHC II. Mainly, two approximate methods for calculating the exciton dynamics have been applied to LHC II, modified Redfield theory<sup>32</sup> and the combined Förster–Redfield approach,<sup>34,37</sup> which interpolates between the two approximations.<sup>58</sup> The time scale for the Chlb/Chla transfer obtained by both methods differs by 1 order of magnitude.<sup>27,32,34–37</sup>

The combined Förster–Redfield theory requires an empirical parameter  $M_{cr}$  for separating the exciton Hamiltonian between a strongly coupled part  $\mathcal{H}_{ex}^{strong}$  with all off-diagonal elements set to zero except those  $|J_{mn}| > M_{cr}$  and the remaining weakly coupled sites.<sup>59</sup> Suggested values for LHC II are  $M_{cr} = 20 \text{ cm}^{-1}$  or smaller.<sup>27,35</sup>

Figure 5 shows the relaxation process from the Chlb band to the Chla band computed with HEOM and different approximate methods. In all cases, the time evolution of the aggregated population at the Chlbs for an initial excitation of the highest exciton eigenstate of the LHC II monomeric unit is depicted. For the combined Förster–Redfield method the initial state is given by the highest eigenstate of  $\mathcal{H}_{ex}^{strong}$  and we corrected a misprint in ref 58 eqs (A3, A4) to comply with the correct eq (50) of ref 59.

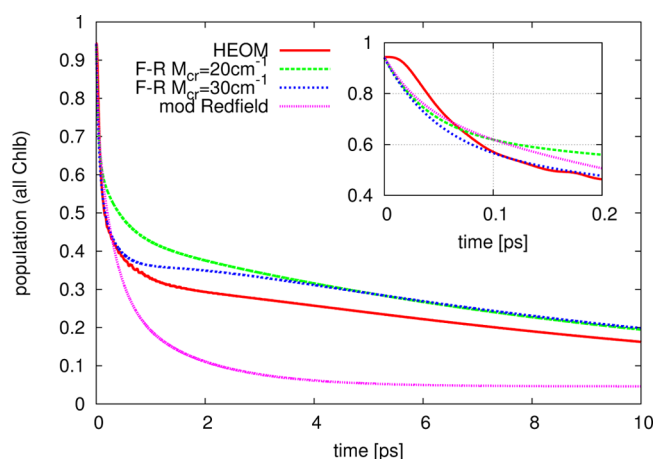


**Figure 5.** Population dynamics in LHC II with initial population of the highest eigenstate of  $\mathcal{H}_{ex}$  for spectral density  $J_{7\text{peaks}}$  at  $T = 300 \text{ K}$  computed with HEOM (*QMaster*,  $N_{\text{max}} = 3$ ) and with combined Förster–Redfield and modified Redfield theories. For the combined method, the initial eigenstate is obtained from  $\mathcal{H}_{ex}^{strong}$ . Shown is the aggregated population of all Chlb as a function of time.

Modified Redfield theory predicts a too fast relaxation and approaches the thermal state already after 6 ps. This is about ten times faster than the HEOM result, which reaches a steady thermal-state after 50 ps. Within the HTA approximation (Appendix B) HEOM converges to 0.034 Chlb steady-state population for  $J_{DL}$ , which differs from the thermal population 0.046. For  $J_{7\text{peaks}}$  and  $t > 4 \text{ ps}$  HTA-HEOM has an offset compared to combined Förster–Redfield theory of about 0.04 aggregated Chlb population.

The dynamics predicted by the combined Förster–Redfield method depends on the choice of  $M_{cr}$ , especially during the first two picoseconds.  $M_{cr} = 30 \text{ cm}^{-1}$  reproduces the initial fast decay of HEOM, while this decay is underestimated for the lower value  $M_{cr} = 20 \text{ cm}^{-1}$ . Both choices for the empirical parameter  $M_{cr}$  reproduce the much slower decay after 4 ps. Overall the combined Förster–Redfield method fits the HEOM results best, but the determination of  $M_{cr}$  can only be verified in hindsight by a comparison with HEOM. None of the approximate methods reproduces the initially nonexponential decay for  $t < 0.1 \text{ ps}$  seen with HEOM (inset Figure 5). The delayed relaxation in LHC II is caused by strong bottleneck sites at Chlb 605 and Chla 604, where around 1–3 ps a transient population accumulates.<sup>32,34</sup> Figure 6 shows the detailed dynamics at these sites and demonstrates the failure of modified Redfield theory. HEOM predicts the largest population at site Chlb 605 (Chla 604) around 2.6 ps (0.6 ps) with a population exceeding 0.1 (0.5). Afterward a slow relaxation sets in and after 10 ps there is still a population about 0.07 (0.25) present at site Chlb 605 (Chla 604). The slow decay of the transient population is causing the delay in the aggregated population dynamics, Figure 5. Modified Redfield theory qualitatively predicts some bottleneck effects at the two sites, but overestimates the energy relaxation. The combined Förster–Redfield method reproduced the bottleneck effects with much better agreement. The error of the combined method depends critically on the choice of  $M_{cr}$ . For the present system parameters  $M_{cr} = 30 \text{ cm}^{-1}$  yields a better agreement with HEOM at the bottleneck site Chlb 605 than  $M_{cr} = 20 \text{ cm}^{-1}$ .

The HEOM result establishes a reliable interband relaxation time scale and shows that the relaxation dynamics proceeds not

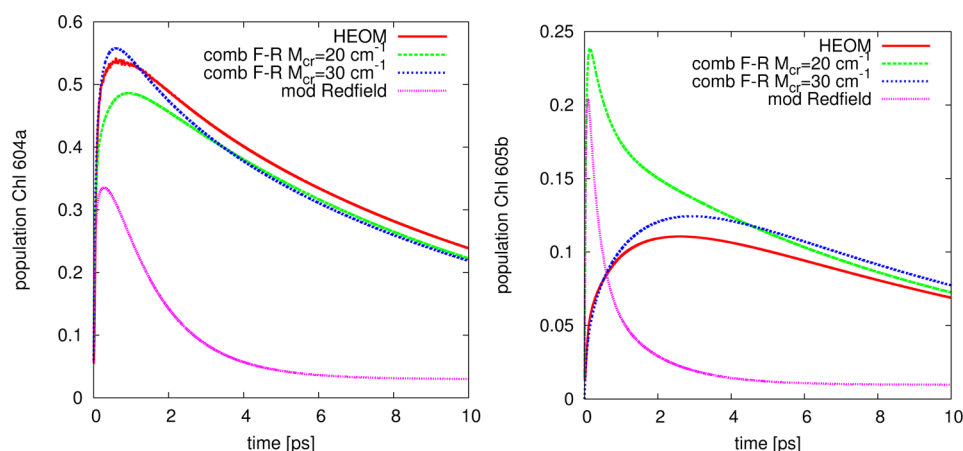


**Figure 6.** Population dynamics at bottleneck sites Chl604 and Chl605 computed with HEOM for  $J_{7\text{peaks}}$  at  $T = 300$  K with  $QMaster$ ,  $N_{\text{max}} = 3$ , combined Förster–Redfield, and modified Redfield theories.

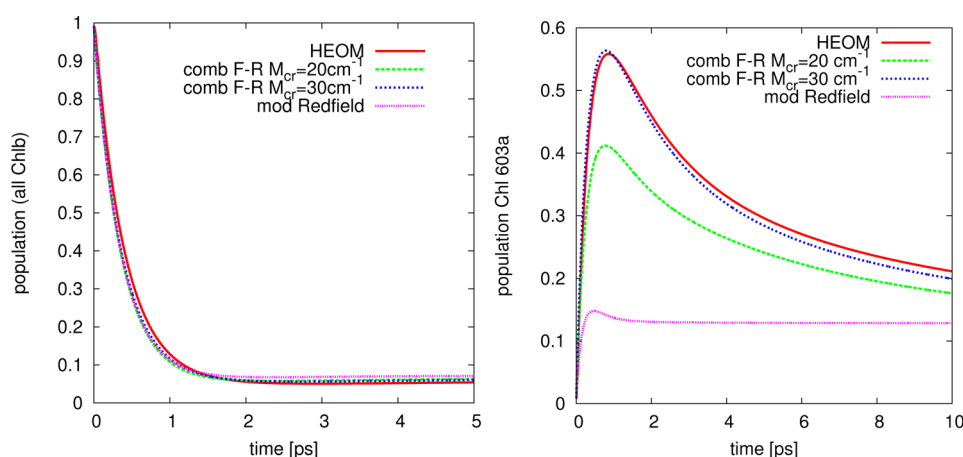


**Figure 7.** Population dynamics in LHC II for the LHC II monomer parameter set given by Müh et al.<sup>38</sup> with initial population of the highest eigenstate of  $\mathcal{H}_{\text{ex}}$  for spectral density  $J_{\text{DL}}$  at  $T = 300$  K computed with HEOM ( $QMaster$ ,  $N_{\text{max}} = 3$ ) and with combined Förster–Redfield and modified Redfield theories. For the combined method, the initial eigenstate is obtained from  $\mathcal{H}_{\text{ex}}^{\text{strong}}$ . Shown is the aggregated population of all Chl b as a function of time (left panel) and the bottleneck site Chl603 (right panel).

between the two approximate limits of Förster or Redfield theory but closer to the predictions of the combined Förster–Redfield method, albeit with a bigger than anticipated value of  $M_{\text{cr}}$ . For the alternative parameter set of the LHC II monomer,<sup>38</sup> the dynamics proceeds faster, and the only bottleneck state is located at Chl a 603 (see Figure 7). As before, the best agreement with the combined Förster–Redfield method at the bottleneck state is obtained for  $M_{\text{cr}} = 30$   $\text{cm}^{-1}$ . A direct comparison with low-temperature data of LHC II spectra is not possible within the HTA approximation. A subpicosecond decay seen in experimental 2D echo spectra<sup>7</sup> and modeled in ref 34 is supported by the  $QMaster$  computation based on the second parameter set.<sup>38</sup>

The combined Förster–Redfield approach relies on rate equations for the projected density matrix operators in the energy-eigenbasis, which brings along several restrictions: (i) the method is limited to very specific initial conditions given in terms of eigenstate populations of  $\mathcal{H}_{\text{ex}}^{\text{strong}}$ ; (ii) it does not treat coherence between exciton states contained in the non-projected density-matrix; and (iii) it neglects nonsecular and non-Markovian effects. The HEOM method is free of these restrictions and allows one to track the exciton dynamics also through a network with the excitation emanating from a

localized site. This initial condition is important for gaining insight into the physical mechanism underlying efficient transfer<sup>15,60</sup> and its relation to the spectral density.<sup>16</sup>

## 6. CONCLUSIONS

With the increasing number of atomistic structure models of photosynthetic complexes, first-principle computations of the excitonic system Hamiltonian become feasible and require accurate and scalable computational methods to compute the ensuing open system dynamics to identify the transport pathways and underlying physical principles. The  $QMaster$  tool harnesses the power of massively parallel processors to accurately simulate the energy transfer in larger light-harvesting complexes with the HEOM method. The modular and platform independent implementation of the OpenCL kernels makes  $QMaster$  a suitable choice for solving the dynamics of open quantum system on existing and emerging many-core processors. Built on top of the accelerated density-matrix dynamics, the easy-to-add functionality during a propagation thread enables the efficient computation of different calculation modes including tracking the population dynamics, computing linear absorption spectra, 2D echo spectra, broadband pump–probe signals,<sup>39,61,62</sup> or transfer efficiency. With a consistent theoretical method at hand, further refinements of



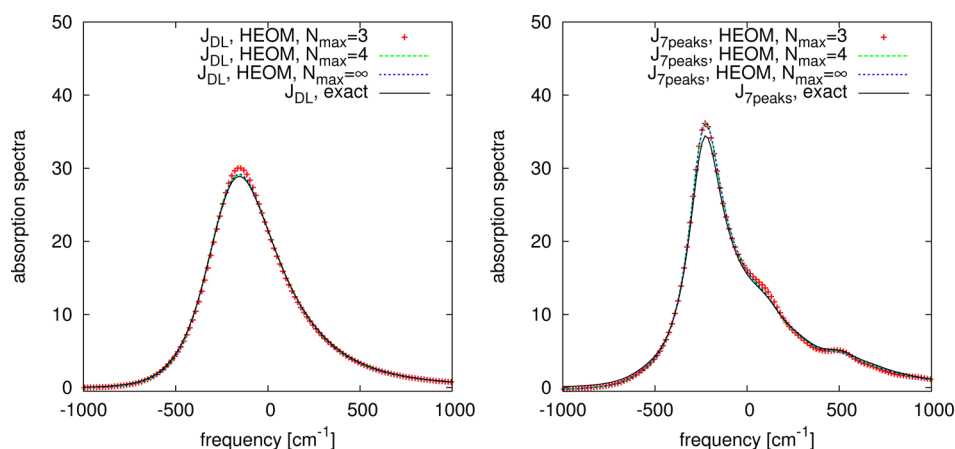


**Figure 8.** Monomer line shape function at  $T = 300$  K for  $J_{DL}$  (left panel) and  $J_{7peaks}$  (right panel). Shown is the exact result and the HEOM calculation at different truncation levels of the hierarchy  $N_{max}$ .

parameters and direct comparisons with experimental data and parameter sets from first-principle computations become feasible.

One important feature which sets *QMaster* apart from other tools is the handling of structured spectral densities. For LHC II specific vibrational modes induce small oscillations on top of the overall relaxation dynamics but do not accelerate the relaxation process. The HEOM results rather emphasizes the importance of interband Chlb/a relaxation due to the coupling to a *continuum* of phonon modes as opposed to a tuning to resonance of specific intramolecular vibrations.

The accurate modeling of the transfer dynamics with *QMaster* resolves the open question whether a Redfield or Förster description is adequate for studying LHC II. HEOM predicts a slow transfer time scale in contrast to the commonly used modified Redfield approximation which underestimates bottleneck effects at Chl 604 and Chl 605. This finding extends to the different parameter set proposed by Müh et al.,<sup>38</sup> which shifts the bottleneck to Chl 603. The combined Förster–Redfield approach yields a reasonable agreement with the HEOM results provided that a larger empirical cutoff parameter  $M_{cr}$  is used than anticipated from earlier works. The choice of  $M_{cr}$  must be validated by *QMaster* in hindsight, depends on the specific realization of the system Hamiltonian and strongly affects the bottleneck states present in LHC II.

## ■ APPENDIX A. PERFORMANCE STRATEGIES ACROSS DIFFERENT OPENCL PLATFORMS

The *QMaster*-tool separates performance critical routines written in OpenCL from the general program flow coded in C++. OpenCL is supported on a wide range of processors spanning hand-held devices to GPUs and many-core CPUs. The underlying performance characteristics and best memory layout and thread-block sizes differ considerably and require choosing the best parameters for a specific device either at run time or beforehand. One important consideration is the number of threads launched simultaneously and the assignment of the thread to the hierarchy of  $N_{matrices}$  density matrices of size  $N_{sites}^2$ . For GPUs the optimal strategy is to launch  $N_{matrices} \times N_{sites}^2$  threads in parallel and to employ local device memory for reusing data across warps. In this scheme, one thread handles one single matrix element. On the many-core CPU we achieve the best performance by launching  $N_{matrices}$  threads, where each thread handles  $N_{sites}^2$  matrix elements and no local memory is used. These two different launch configurations do not require

to change the underlying data layout in the device-memory, which stores in both cases an array of  $N_{matrices}$ , with each array member holding  $N_{sites}^2$  matrix elements consecutively.

## ■ APPENDIX B. MONOMER ABSORPTION SPECTRA

The convergence and numerical accuracy of the HEOM method is conveniently tested by comparing the absorption spectra for a monomeric two-level system computed with HEOM to the analytically known result.<sup>50,51</sup> The absorption spectra  $I(\omega)$  of a monomer with excitation frequency  $\omega_{eg}$  is given by the Fourier transform of the line shape function<sup>52</sup>

$$I(\omega) = \frac{1}{\pi} \Re \int_0^\infty dt \exp(-g(t) + i(\omega - \omega_{eg} - \lambda)t) \quad (14)$$

with  $g(t)$  obtained by integrating over the spectral density

$$g(t) = -\frac{1}{2\pi} \int_{-\infty}^\infty d\omega \frac{J(\omega)}{\omega^2} (1 + \coth(\beta\hbar\omega/2)) (e^{-i\omega t} + i\omega t - 1) \quad (15)$$

For the structured spectral density eq 7,  $g(t)$  can be derived in terms of the hypergeometric function  ${}_2F_1$ . At the physiological temperature-range encountered in light-harvesting complexes, HEOM uses the high-temperature approximation (HTA) for  $g(t)$  to avoid a memory-consuming Matsubara expansion

$$g_{HTA}(t) = \sum_{\nu_{\pm} = \nu \pm i\Omega} \int_0^t d\tau \int_0^\tau d\tau_2 \left[ \frac{2e^{-\tau_2\nu_{\pm}\lambda}}{\beta\hbar} - \frac{4e^{-\tau_2\nu_{\pm}\lambda}}{4\pi^2 - \beta^2\nu_{\pm}^2\hbar^2} + \frac{4\beta\nu_{\pm}\hbar\delta(\tau_2)}{4\pi^2 - \beta^2\nu_{\pm}^2\hbar^2} - i\lambda\nu_{\pm}e^{-\nu_{\pm}\tau_2} \right] \quad (16)$$

The HEOM system is terminated at a certain truncation depth  $N_{max}$ , resulting in an implicit  $N_{max}$  representation of  $g_{HTA}^{N_{max}}(t)$ , with  $g_{HTA}^{N_{max}}(t) \equiv g_{HTA}(t)$ . As shown in Figure 8, already at a truncation level of  $N_{max} = 3$  the, monomer line shapes are in good agreement with the HTA and exact expressions at  $T = 300$  K. For the long-time evolution the HTA leads to a slight offset of the populations from the true thermal state, which overestimates the final Chla population.

## ■ ASSOCIATED CONTENT

### Supporting Information

The Supporting Information lists the site energies and intersite couplings of the LHC II monomeric unit compiled from ref. 35 This material is available free of charge via the Internet at <http://pubs.acs.org/>.



## AUTHOR INFORMATION

### Corresponding Authors

\*E-mail: christoph.kreisbeck@physik.hu-berlin.de.

\*E-mail: kramer@mci.sdu.dk.

\*E-mail: aspuru@chemistry.harvard.edu.

### Notes

The authors declare no competing financial interest.

## ACKNOWLEDGMENTS

We thank Nvidia for support via the Harvard CUDA Center of Excellence. C.K. and A.A.-G. are supported by the DARPA grant N66001-10-1-4059, and A.A.-G. by the Center for Excitonics, an Energy Frontier Research Center funded by the U.S. Department of Energy, Office of Science, Office of Basic Energy Sciences, under Award Number DESC0001088. T.K. acknowledges support by the Heisenberg program of the DFG (KR2889/5-1). We thank A. Reinefeld and F. Wende at the Zuse Institute Berlin (ZIB) for computing time and helpful discussions.

## REFERENCES

- (1) Leegwater, J. A. Coherent versus Incoherent Energy Transfer and Trapping in Photosynthetic Antenna Complexes. *J. Phys. Chem.* **1996**, *100*, 14403.
- (2) Amerongen, H. V.; Valkunas, L.; van Grondelle, R. *Photosynthetic Excitons*; World Scientific: Singapore, 2000; pp 47–72.
- (3) May, V.; Kühn, O. *Charge and Energy Transfer Dynamics in Molecular Systems*; Wiley-VCH: Weinheim, 2004; pp 405–451.
- (4) Brixner, T.; Stenger, J.; Vaswani, H. M.; Cho, M.; Blankenship, R. E.; Fleming, G. R. Two-dimensional Spectroscopy of Electronic Couplings in Photosynthesis. *Nature* **2005**, *434*, 625–628.
- (5) Engel, G. S.; Calhoun, T. R.; Read, E. L.; Ahn, T.-K.; Mancal, T.; Cheng, Y.-C.; Blankenship, R. E.; Fleming, G. R. Evidence For Wavelike Energy Transfer Through Quantum Coherence In Photosynthetic Systems. *Nature* **2007**, *446*, 782–786.
- (6) Panitchayangkoon, G.; Hayes, D.; Fransted, K. A.; Caram, J. R.; Harel, E.; Wen, J.; Blankenship, R. E.; Engel, G. S. Long-lived Quantum Coherence in Photosynthetic Complexes at Physiological Temperature. *Proc. Natl. Acad. Sci. U.S.A.* **2010**, *107*, 12766–12770.
- (7) Calhoun, T. R.; Ginsberg, N. S.; Schlau-Cohen, G. S.; Cheng, Y.-C.; Ballottari, M.; Bassi, R.; Fleming, G. R. Quantum Coherence Enabled Determination of the Energy Landscape in Light-Harvesting Complex II. *J. Phys. Chem. B* **2009**, *113*, 16291–16295.
- (8) Schlau-Cohen, G. S.; Ishizaki, A.; Calhoun, T. R.; Ginsberg, N. S.; Ballottari, M.; Bassi, R.; Fleming, G. R. Elucidation of the timescales and origins of quantum electronic coherence in LHCII. *Nat. Chem.* **2012**, *4*, 389–395.
- (9) Kreisbeck, C.; Kramer, T. Long-Lived Electronic Coherence in Dissipative Exciton Dynamics of Light-Harvesting Complexes. *J. Phys. Chem. Lett.* **2012**, *3*, 2828–2833.
- (10) Kreisbeck, C.; Kramer, T.; Aspuru-Guzik, A. Disentangling Electronic and Vibronic Coherences in Two-Dimensional Echo Spectra. *J. Phys. Chem. B* **2013**, *117*, 9380–9385.
- (11) Mohseni, M.; Rebentrost, P.; Lloyd, S.; Aspuru-Guzik, A. Environment-assisted Quantum Walks in Photosynthetic Energy Transfer. *J. Chem. Phys.* **2008**, *129*, 174106.
- (12) Rebentrost, P.; Mohseni, M.; Kassal, I.; Lloyd, S.; Aspuru-Guzik, A. Environment-assisted Quantum Transport. *New J. Phys.* **2009**, *11*, 033003.
- (13) Ishizaki, A.; Fleming, G. R. Theoretical examination of quantum coherence in a photosynthetic system at physiological temperature. *Proc. Natl. Acad. Sci. U.S.A.* **2009**, *106*, 17255.
- (14) Ishizaki, A.; Fleming, G. R. Unified treatment of quantum coherent and incoherent hopping dynamics in electronic energy transfer: Reduced hierarchy equation approach. *J. Chem. Phys.* **2009**, *130*, 234111.
- (15) Kreisbeck, C.; Kramer, T.; Rodríguez, M.; Hein, B. High-Performance Solution of Hierarchical Equations of Motion for Studying Energy Transfer in Light-Harvesting Complexes. *J. Chem. Theory Comput.* **2011**, *7*, 2166–2174.
- (16) Kramer, T.; Kreisbeck, C. Modelling excitonic-energy transfer in light-harvesting complexes. *AIP Conf. Proc.* **2014**, *1575*, 111–135.
- (17) Christensson, N.; Kauffmann, H. F.; Pullerits, T.; Mancal, T. Origin of Long Lived Coherences in Light-Harvesting Complexes. *J. Phys. Chem. B* **2012**, *116*, 7449–7454.
- (18) Strümpfer, J.; Schulten, K. Light harvesting complex II B850 excitation dynamics. *J. Chem. Phys.* **2009**, *131*, 225101.
- (19) Strümpfer, J.; Schulten, K. Open Quantum Dynamics Calculations with the Hierarchy Equations of Motion on Parallel Computers. *J. Chem. Theory Comput.* **2012**, *8*, 2808–2816.
- (20) Hein, B.; Kreisbeck, C.; Kramer, T.; Rodríguez, M. Modelling of Oscillations in Two-Dimensional Echo-Spectra of the Fenna–Matthews–Olson Complex. *New J. Phys.* **2012**, *14*, 023018.
- (21) Kreisbeck, C.; Kramer, T. Exciton Dynamics Lab for Light-Harvesting Complexes (GPU-HEOM); DOI:10.4231/D3RB6W248. Online at <https://nanohub.org/resources/gpuheompop> (accessed July 13, 2014).
- (22) Liu, Z.; Yan, H.; Wang, K.; Kuang, T.; Zhang, J.; Gui, L.; An, X.; Chang, W. Crystal structure of spinach major light-harvesting complex at 2.72 Å resolution. *Nature* **2004**, *428*, 287–292.
- (23) Kühlbrandt, W.; Wang, D. N.; Fujiyoshi, Y. Atomistic model of plant light-harvesting complex by electron crystallography. *Nature* **1994**, *367*, 614–621.
- (24) Kouřil, R.; Dekker, J. P.; Boekema, E. J. Supramolecular organization of photosystem II in green plants. *Biochim. Biophys. Acta, Bioenerg.* **2012**, *1817*, 2–12.
- (25) Duffy, C. D. P.; Valkunas, L.; Ruban, A. V. Light-harvesting processes in the dynamic photosynthetic antenna. *Phys. Chem. Chem. Phys.* **2013**, *15*, 18752–18770.
- (26) Novoderezhkin, V. I.; Palacios, M. A.; van Amerongen, H.; van Grondelle, R. Energy-Transfer Dynamics in the LHCII Complex of Higher Plants: Modified Redfield Approach. *J. Phys. Chem. B* **2004**, *108*, 10363–10375.
- (27) Novoderezhkin, V. I.; van Grondelle, R. Physical origins and models of energy transfer in photosynthetic light-harvesting. *Phys. Chem. Chem. Phys.* **2010**, *12*, 7352–7365.
- (28) Nalbach, P.; Mujica-Martinez, C. A.; Thorwart, M. Vibronic speed-up of the excitation energy transfer in the Fenna–Matthews–Olson complex. arXiv e-print archive at arXiv:1311.6363 2013 (accessed July 13, 2014).
- (29) O'Reilly, E. J.; Olaya-Castro, A. Non-classicality of the molecular vibrations assisting exciton energy transfer at room temperature. *Nat. Commun.* **2014**, *5*, 3012.
- (30) Nalbach, P.; Thorwart, M. The role of discrete molecular modes in the coherent exciton dynamics in FMO. *J. Phys. B: At., Mol. Opt. Phys.* **2012**, *45*, 154009.
- (31) Dijkstra, A. G.; Cao, J.; Fleming, G. R. Exciton dynamics in the presence of colored noise from underdamped vibrations. arXiv e-print archive at arXiv:1309.4910 2013 (accessed July 13, 2014).
- (32) Novoderezhkin, V. I.; Palacios, M. A.; van Amerongen, H.; van Grondelle, R. Excitation dynamics in the LHCII complex of higher plants: modeling based on the 2.72 Å crystal structures. *J. Phys. Chem. B* **2005**, *109*, 10493–10504.
- (33) Abramavicius, D.; Mukamel, S. Energy-transfer and charge-separation pathways in the reaction center of photosystem II revealed by coherent two-dimensional optical spectroscopy. *J. Chem. Phys.* **2010**, *133*, 184501.
- (34) Renger, T.; Madjet, M.; Knorr, A.; Müh, F. How the molecular structure determines the flow of excitation energy in plant light-harvesting complex II. *J. Plant Physiol.* **2011**, *168*, 1497–1509.
- (35) Novoderezhkin, V.; Marin, A.; van Grondelle, R. Intra- and inter-monomeric transfers in the light harvesting LHCII complex: the Redfield–Förster picture. *Phys. Chem. Chem. Phys.* **2011**, *13*, 17093–17103.

- (36) Novoderezhkin, V.; van Grondelle, R. Spectra and Dynamics in the B800 Antenna: Comparing Hierarchical Equations, Redfield and Förster Theories. *J. Phys. Chem. B* **2013**, *117*, 11076–11090.
- (37) Novoderezhkin, V. Combined Förster–Redfield theory for modeling energy transfer in plant photosynthesis antenna complexes. *Biol. Membr.* **2012**, *29*, 367–373.
- (38) Müh, F.; Madjet, M. E.-A.; Renger, T. Structure-based identification of energy sinks in plant light-harvesting complex II. *J. Phys. Chem. B* **2010**, *114*, 13517–13535.
- (39) Jankowiak, R.; Reppert, M.; Zazubovich, V.; Pieper, J.; Reinot, T. Site selective and single complex laser-based spectroscopies: a window on excited state electronic structure, excitation energy transfer, and electron–phonon coupling of selected photosynthetic complexes. *Chem. Rev.* **2011**, *111*, 4546–4598.
- (40) Olsina, J.; Kramer, T.; Kreisbeck, C.; Mancal, T. Exact Stochastic Unraveling of an Optical Coherence Dynamics by Cumulant Expansion. arXiv e-print archive at arXiv:1309.0749 2013, (accessed July 13, 2014).
- (41) Deumens, E. Method development in atomistic computation: past and future. *Mol. Phys.* **2010**, *108*, 3249–3257.
- (42) Leang, S. S.; Rendell, A. P.; Gordon, M. S. Quantum Chemical Calculations using Accelerators: Migrating Matrix Operations to the NVIDIA Kepler GPU and the Intel Xeon Phi. *J. Chem. Theory Comput.* **2014**, *10*, 908–912.
- (43) Playne, D. P.; Hawick, K. A. Comparison of GPU architectures for asynchronous communication with finite-differencing applications. *Concurrency and Computation: Practice and Experience* **2012**, *24*, 73–83.
- (44) Peterman, E. J.; Pullerits, T.; van Grondelle, R.; van Amerongen, H. Electron-phonon coupling and vibronic fine structure of light-harvesting complex II of green plants: temperature dependent absorption and high-resolution fluorescence spectroscopy. *J. Phys. Chem. B* **1997**, *101*, 4448–4457.
- (45) Bennett, D. I. G.; Amarnath, K.; Fleming, G. R. A Structure-Based Model of Energy Transfer Reveals the Principles of Light Harvesting in Photosystem II Supercomplexes. *J. Am. Chem. Soc.* **2013**, *135*, 9164–9173.
- (46) Tanimura, Y.; Mukamel, S. Optical Stark spectroscopy of a Brownian oscillator in intense fields. *J. Phys. Soc. Jpn.* **1994**, *63*, 66–77.
- (47) Tanimura, Y. Reduced hierarchy equations of motion approach with Drude plus Brownian spectral distribution: Probing electron transfer processes by means of two-dimensional correlation spectroscopy. *J. Chem. Phys.* **2012**, *137*, 22A550.
- (48) Tanimura, Y.; Kubo, R. Time Evolution of a Quantum System in Contact with a Nearly Gaussian-Markoffian Noise Bath. *J. Phys. Soc. Jpn.* **1989**, *58*, 101–114.
- (49) Shi, Q.; Chen, L.; Nan, G.; Xu, R.-X.; Yan, Y. Efficient hierarchical Liouville space propagator to quantum dissipative dynamics. *J. Chem. Phys.* **2009**, *130*, 084105.
- (50) Lax, M. The Franck-Condon Principle and Its Application to Crystals. *J. Chem. Phys.* **1952**, *20*, 1752–1760.
- (51) Kubo, R.; Toyozawa, Y. Application of the method of generating function to radiative and non-radiative transitions of a trapped electron in a crystal. *Prog. Theor. Phys.* **1955**, *13*, 160–182.
- (52) Mukamel, S. Non-Markovian theory of molecular relaxation. I. Vibrational relaxation and dephasing in condensed phases. *Chem. Phys.* **1979**, *37*, 33–47.
- (53) Knox, R. S.; Small, G. J.; Mukamel, S. Low-temperature zero phonon lineshapes with various Brownian oscillator spectral densities. *Chem. Phys.* **2002**, *281*, 1–10.
- (54) Tiwari, V.; Peters, W. K.; Jonas, D. M. Electronic resonance with anticorrelated pigment vibrations drives photosynthetic energy transfer outside the adiabatic framework. *Proc. Natl. Acad. Sci. U.S.A.* **2013**, *110*, 1203–1208.
- (55) Kell, A.; Feng, X.; Reppert, M.; Jankowiak, R. On the shape of the phonon spectral density in photosynthetic complexes. *J. Phys. Chem. B* **2013**, *117*, 7317–7323.
- (56) Kell, A.; Acharya, K.; Blankenship, R. E.; Jankowiak, R. On destabilization of the Fenna–Matthews–Olson complex of *Chlorobaculum tepidum*. *Photosynth. Res.* **2014**, *120*, 323–329.
- (57) Plenio, M. B.; Huelga, S. F. Dephasing-assisted Transport: Quantum Networks and Biomolecules. *New J. Phys.* **2008**, *10*, 113019.
- (58) Yang, M.; Damjanović, A.; Vaswani, H. M.; Fleming, G. R. Energy Transfer in Photosystem I of Cyanobacteria *Synechococcus elongatus*: Model Study with Structure-Based Semi-Empirical Hamiltonian and Experimental Spectral Density. *Biophys. J.* **2003**, *85*, 140–158.
- (59) Yang, M.; Fleming, G. R. Influence of phonons on exciton transfer dynamics: comparison of the Redfield, Förster, and modified Redfield equations. *Chem. Phys.* **2002**, *282*, 163–180.
- (60) Wu, J.; Liu, F.; Ma, J.; Silbey, R. J.; Cao, J. Efficient energy transfer in light-harvesting systems: Quantum-classical comparison, flux network, and robustness analysis. *J. Chem. Phys.* **2012**, *137*, 174111.
- (61) Hamm, P.; Zanni, M. T. *Concepts and Methods of 2D Infrared Spectroscopy*; Cambridge University Press: Cambridge, 2011; pp 1–252.
- (62) Yuen-Zhou, J.; Krich, J. J.; Aspuru-Guzik, A. A witness for coherent electronic vs vibronic-only oscillations in ultrafast spectroscopy. *J. Chem. Phys.* **2012**, *136*, 234501.